

See discussions, stats, and author profiles for this publication at: <https://www.researchgate.net/publication/231396405>

Interpolated variational transition-state theory and semiclassical tunneling calculations of the rate constant of the reaction hydroxyl + ethane at 200–3000 K

ARTICLE in THE JOURNAL OF PHYSICAL CHEMISTRY · JANUARY 1994

Impact Factor: 2.78 · DOI: 10.1021/j100054a023

CITATIONS

59

READS

11

2 AUTHORS:



Vasilios Melissas

University of Ioannina

39 PUBLICATIONS 942 CITATIONS

SEE PROFILE



Donald Truhlar

University of Minnesota Twin Cities

1,342 PUBLICATIONS 79,615 CITATIONS

SEE PROFILE

Interpolated Variational Transition-State Theory and Semiclassical Tunneling Calculations of the Rate Constant of the Reaction $\text{OH} + \text{C}_2\text{H}_6$ at 200–3000 K

Vasilios S. Melissas and Donald G. Truhlar*

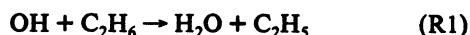
Department of Chemistry and Supercomputer Institute, University of Minnesota,
Minneapolis, Minnesota, 55455-0431

Received: September 7, 1993; In Final Form: October 29, 1993*

Ab initio molecular orbital calculations were carried out for the reaction $\text{OH} + \text{C}_2\text{H}_6 \rightarrow \text{H}_2\text{O} + \text{C}_2\text{H}_5$ using second-order Møller–Plesset perturbation theory and employing a very large basis set. Correlation energy is found to play an important role in determining the barrier height of the saddle point and also the geometry and the vibrational frequencies of both the transition state and the equilibrium points. The final calculated values for the forward and reverse classical barrier heights are 4.0 and 21.6 kcal/mol, respectively. These have been used to treat the kinetics of the reaction in the temperature range from 200 to 3000 K by using interpolated canonical variational transition-state theory and the centrifugal-dominant, small-curvature tunneling approximation, including information at the reactants, products, transition state, and one extra point along the minimum energy path. The calculated rate constants agree well with experiment over a wide temperature range.

1. Introduction

Of the numerous radicals of relevance to both atmospheric and combustion chemistry, the hydroxyl radical plays a particularly important role. For example, reaction with the hydroxyl radical is the primary loss channel for alkanes in the stratosphere, a loss mechanism which receives some competition from photolytic decomposition of alkanes by solar UV light.¹ The hydroxyl radical is also a principal chain carrier in hydrocarbon combustion. Thus, the reaction of OH with ethane, the simplest hydrocarbon after methane,



is of particular importance in both combustion and atmospheric applications, and its theoretical investigation is very interesting. Many experimental studies of the kinetics of this reaction have been reported, using both absolute and, especially at elevated temperatures, relative rate methods.^{1–22} The results have been evaluated and combined into four recommended expressions^{14,15,19,21}—the first three being three-parameter fits and the last a two-parameter one. The most recent recommended expression²¹ covers the temperature range from 210 to 380 K, and the most reliable three-parameter one¹⁹ covers the temperature range from 226 to 800 K. For the overlapping temperature range of the two fits, the low-temperature fit²¹ is considered more reliable. An Arrhenius plot of the three-parameter recommended expression¹⁹ shows significant curvature at temperatures below about 700 K, and this may be an indication that tunneling plays an important role in this temperature range; however, no curvature is included in the Arrhenius fit of the low-temperature data.²¹ The lack of an analytical potential energy function or of any *ab initio* calculations has impeded theoretical progress in dynamical studies of reaction (R1).

In the present study, we report accurate *ab initio* calculations for the structures, energetics, and vibrational frequencies of the reactants, products, and saddle point of reaction (R1) and we also report results at the same level for an extra point along the minimum energy path (MEP^{23–25}). The extra point is displaced from the saddle point a small distance toward the products. Then, we use these calculations with a recently proposed approximation scheme²⁷ for quantized variational transition-state theory (VTST) and semiclassical tunneling calculations to predict reaction rate constants. This scheme is called interpolated VTST or IVTST,

and it was recently applied to the reactions of $\text{OH} + \text{CH}_4 \rightarrow \text{H}_2\text{O} + \text{CH}_3$ ²⁸ and $\text{OH} + \text{CD}_4 \rightarrow \text{HDO} + \text{CD}_3$ ²⁹ with *ab initio* surface information. The resulting rate constants and non-Arrhenius behavior for those reactions are in good agreement with experiments. In the present work, we use the first-order global version of interpolated canonical variational transition-state theory with small-curvature tunneling (SCT) corrections to predict reaction rate constants and activation energies. The SCT calculations are based on the relatively new centrifugal-dominant, small-curvature semiclassical adiabatic ground-state^{30,31} (CD-SCSAG, or, for short, small-curvature tunneling, SCT) method, and we also compare them to calculations with a zero-curvature tunneling^{24,26,31,32} (ZCT) calculation.

2. Computational Methodology

For the electronic structure calculations, we employ restricted Hartree–Fock (RHF) theory³³ for closed-shell systems (H_2O , C_2H_6) and unrestricted Hartree–Fock (UHF) theory³³ for open-shell systems (OH, C_2H_5 , the saddle point, and the extra point along the MEP). Second-order Møller–Plesset perturbation theory³³ (MP2), unrestricted MP2³³ (UMP2), and UMP2 with spin projection^{34,35} (PMP2//UMP2) are employed, based on these RHF and UHF reference wave functions.

The motivation of the spin-projection method arises from previous studies where the transition structures calculated at the UHF level are affected by a considerable amount of spin contamination,³⁵ and as a result, the reaction barriers can be overestimated by up to 10 kcal/mol when correlation corrections are calculated by unrestricted Møller–Plesset perturbation theory. In this rest of this paper, we omit the U when referring to UHF and UMP2 calculations. Thus, HF denotes HF or UHF depending on whether the number of electrons is even or odd, respectively, and likewise for MP2.

All correlation energy in MP2 calculations is scaled³⁶ (scaling all correlation energy is abbreviated SAC) to yield an improved calculation of the barrier height at the MP2 optimized structure. This is called the MP-SAC2//MP2 level. The total electronic energy in the MP-SAC2//MP2 calculations is written as³⁶

$$E_{\text{MP-SAC2//MP2}} = E_{\text{HF}} + \frac{E_{\text{MP2}} - E_{\text{HF}}}{\mathcal{F}_2} \quad (1)$$

where \mathcal{F}_2 is a scaling factor which is assumed to be independent of geometry for a given system and HF denotes RHF or UHF,

* Abstract published in *Advance ACS Abstracts*, December 15, 1993.

depending on the system. The motivation of the SAC method for large basis sets, such as used for the calculations here, is to make the calculated exoergicity of the reaction agree perfectly with experiment so that the treatment of reactants and products is balanced and a set of forward and reverse rate constants consistent with the equilibrium constant can be obtained. The \mathcal{F}_2 factor can be computed from the accurate, MP2, and HF binding energies for each bond type. Further details of the SAC method may be found in the original work³⁶ and our previous application.²⁸

A correlation-consistent polarized-valence triple- ζ (cc-pVTZ) basis set of Dunning³⁷ is the starting point for our large-scale calculations. For H, this is a (5s2p1d) primitive Gaussian basis set contracted to [3s2p1d] (18 primitive functions/14 contracted functions), whereas for C and O, it is a (10s5p2d1f) primitive set contracted to [4s3p2d1f] (60 primitive functions/30 contracted functions). Pure d and f functions are used in the d and f shells, i.e., the d functions have five components and the f functions seven. We used this basis unchanged for some calculations, although for others, we used an adjusted version of this basis set where the same \mathcal{F}_2 scaling factor applies to the computed dissociation energies of both the C-H and O-H bonds. This adjusted basis, called second-adjusted cc-pVTZ (adj2-cc-pVTZ), is explained in detail in section 4. The basis set was adjusted in order to treat electron correlation in the forming and breaking bonds of reaction (R1) on an equal footing as required to obtain an accurate barrier height for both directions of reaction.

The geometries of all stationary points, i.e., minimum energy structures and the saddle point, were fully optimized at the HF and MP2 levels of theory with the adj2-cc-pVTZ basis set. In addition, the geometries of all equilibrium points, i.e., reactants and products, were fully optimized at the HF/cc-pVTZ and MP2/cc-pVTZ levels of theory. We used C_1 point group symmetry for each species as the initial geometry of the optimization procedure, and we fully optimized³⁸ all the Z-matrix^{39,40} parameters. Internal coordinates⁴¹ were selected for the geometry optimization, since the total energy is invariant to overall translation and rotation. The resulting point group symmetries at all available levels are $C_{\infty v}$ for OH, C_{2v} for H_2O , C_s for C_2H_5 , and D_{3d} for C_2H_6 , whereas the symmetry is C_s for the C_2H_5 -H-OH saddle point at the HF/adj2-cc-pVTZ level and C_1 at the MP2/adj2-cc-pVTZ level. The symmetry is C_1 for the extra point along the reaction path on the product side of the saddle point (no optimization is required for this point).

Vibrational frequencies were calculated at four levels for all equilibrium points, in particular at the HF and MP2 levels for both the cc-pVTZ and adj2-cc-pVTZ basis sets. However, only HF/adj2-cc-pVTZ and MP2/adj2-cc-pVTZ frequency calculations were carried out for the saddle point, and only MP2/adj2-cc-pVTZ frequencies were calculated at the extra point along the MEP.

Since unrestricted HF wave functions are not spin eigenfunctions, we have monitored the expectation value of S^2 in all unrestricted HF and MP2 wave functions (where S denotes electron spin angular momentum in units of \hbar). For doublets, S^2 was always in the range 0.756–0.796, where 0.750 is the correct value. (For completeness, we note that the largest deviation of S^2 , 0.046, from the correct value corresponds to the saddle point calculation at the HF/adj2-cc-pVTZ level.) Although this amount of spin contamination is not considered severe, we mention that the forward barrier height of reaction (R1) at the MP2/adj2-cc-pVTZ level—for which spin projection is not included—is larger by 1.80 kcal/mol than its value at the PMP2//MP2/adj2-cc-pVTZ level.

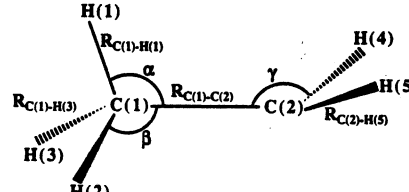
Various amounts of memory and disk space were required for the optimization and frequencies calculations of the various species under study. Most of the optimization and frequencies calculations required no more than 12 megawords of memory and 2

TABLE 1: Optimized Minimum Energy Structures (bond lengths in Å, bond angles in degrees) for OH and H_2O

level/basis set	OH ($C_{\infty v}$)	H_2O (C_{2v})	
	O-H	O-H	HOH
HF/cc-pVTZ	0.9512	0.9406	106.00
HF/adj2-cc-pVTZ	0.9512	0.9407	105.96
MP2/cc-pVTZ	0.9659	0.9575	103.66
MP2/adj2-cc-pVTZ	0.9667	0.9586	103.57
experimental	0.9706 ^a	0.9576 ^b	104.48 ^b

^a Reference 48. ^b Reference 49.

TABLE 2: Optimized Minimum Energy Structures (bond lengths in Å, bond and dihedral angles in degrees) for C_2H_5 (C_s)



level/basis set	HF/cc-pVTZ and HF/adj2-cc-pVTZ	MP2/cc-pVTZ and MP2/adj2-cc-pVTZ
$R_{C(1)-C(2)}$	1.4948	1.4809
$R_{C(1)-H(1)}$	1.0893	1.0918
$R_{C(1)-H(3)}$	1.0838	1.0851
$R_{C(2)-H(5)}$	1.0734	1.0728
α	111.57	111.60
β	111.34	111.55
γ	120.47	120.67
ϕ_1^a	119.66	119.42
ϕ_2^b	82.57	84.54

^a ϕ_1 is the dihedral angle between the H(2)-C(1)-C(2) and C(1)-C(2)-H(1) planes. ^b ϕ_2 is the dihedral angle between the H(4)-C(2)-C(1) and C(2)-C(1)-H(1) planes.

gigabytes of disk space; however, the MP2 frequency calculations in the saddle point region required 18 megawords of memory and 8 gigabytes of disk space. Direct^{42,43} SCF methods were used in all our calculations, recomputing the two-electron integrals as needed. Moreover, analytic Hessian calculations were performed at both the HF⁴⁴ and MP2⁴⁵ levels of theory.

A mass-scaled coordinate system^{26,46} was defined as

$$x_{i\gamma} = (m_i/\mu)^{1/2} R_{i\gamma} \quad (2)$$

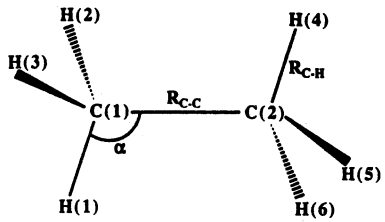
where m_i is the mass of atom i , μ is the reduced mass of the relative translational motion of reactants, which in this case equals 10.858 amu, and $R_{i\gamma}$ is a Cartesian coordinate with $\gamma = x, y$, or z . The geometry of a nonstationary point along the MEP on the product side of the saddle point was determined by taking a step of length 0.005 a_0 in the direction of the mass-scaled eigenvector corresponding to the saddle point imaginary frequency.

All *ab initio* calculations were carried out using the GAUSS-92⁴⁷ program on the Cray X-MP/EA and Cray Y-MP8/864 computers at the Minnesota and San Diego Supercomputer Centers, respectively.

3. Structures and Vibrational Frequencies

The optimized geometries for the minimum energy structures are given in Tables 1–3. We found that the HF bond lengths of both closed- and open-shell species are generally shorter than the experimental values^{48–50} (which are available only for OH, H_2O , and C_2H_6), but by at most 2%. However, when electron correlation is included at the MP2 level, bond lengths agree with the experimental data within 0.5%.

Vibrational analysis was performed at all points, and the vibrational frequencies for the equilibrium species calculated at

TABLE 3: Optimized Minimum Energy Structures (bond lengths in Å, bond and dihedral angles in degrees) for C_2H_6 (D_{3d})


level/ basis set	HF/cc-pVTZ and HF/adj2-cc-pVTZ	MP2/cc-pVTZ and MP2/adj2-cc-pVTZ	experimental ^a
R_{C-C}	1.5245	1.5177	1.5243
R_{C-H}	1.0841	1.0850	1.0895
α	111.21	111.17	111.95
ϕ_1^b	120.00	120.00	120.00

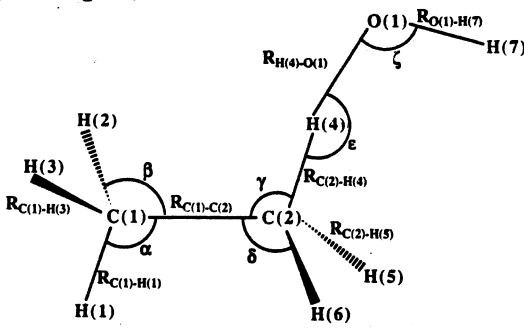
^a Reference 50. ^b ϕ_1 is the dihedral angle between the H(2)-C(1)-C(2) and C(1)-C(2)-H(1) planes.

TABLE 4: Vibrational Frequencies (cm⁻¹) of the Equilibrium Structures

mode	sym- metry	HF/ cc- pVTZ	HF/ adj2-cc- pVTZ	MP2/ cc- pVTZ	MP2/ adj2-cc- pVTZ	har- monic (exp)	funda- mental (exp)
OH							
1	σ_g	4039	4040	3837	3814 (5.45) ^a	3735 ^b	3570 ^b
H₂O							
1	a_1	4127	4127	3872	3847	3834 ^c	3651 ^b
2	a_1	1753	1755	1650	1646	1649 ^c	1595 ^b
3	b_2	4227	4226	3993	3963 (13.52) ^a	3935 ^c	3756 ^b
C₂H₅							
1	a'	3264	3264	3239	3239	n/a ^a	3033 ^e
2	a'	3180	3180	3127	3127	n/a ^a	2920 ^e
3	a'	3113	3113	3049	3049	n/a ^a	2842 ^e
4	a'	1603	1603	1520	1520	n/a ^a	1440 ^e
5	a'	1582	1582	1505	1505	n/a ^a	n/a
6	a'	1523	1523	1419	1419	n/a ^a	1366 ^e
7	a'	1100	1100	1098	1098	n/a ^a	1138 ^e
8	a'	1068	1068	998	998	n/a ^a	n/a
9	a'	465	465	488	488	n/a ^a	540 ^e
10	a''	3362	3362	3330	3330	n/a ^a	3112 ^e
11	a''	3214	3214	3169	3169	n/a ^a	2987 ^e
12	a''	1600	1600	1516	1516	n/a ^a	1440 ^e
13	a''	1294	1294	1218	1218	n/a ^a	1175 ^e
14	a''	861	861	825	825	n/a ^a	n/a
15	a''	162	162	135	135 (38.08) ^a	n/a ^a	n/a
C₂H₆							
1	a_{1g}	3158	3158	3101	3101	3043 ^f	2954 ^g
2	a_{1g}	1548	1548	1441	1441	1449 ^f	1388 ^g
3	a_{1g}	1049	1049	1038	1038	1016 ^f	995 ^g
4	a_{1u}	328	328	343	343	303 ^f	289 ^g
5	a_{2u}	3152	3152	3099	3099	3061 ^f	2896 ^g
6	a_{2u}	1522	1522	1418	1418	1438 ^f	1379 ^g
7	e_g	3194	3194	3158	3158	3175 ^f	2969 ^h
8	e_g	1614	1614	1535	1535	1552 ^f	1468 ^g
9	e_g	1323	1323	1239	1239	1246 ^f	1190 ^g
10	e_u	3222	3222	3180	3180	3140 ^f	2985 ^g
11	e_u	1619	1619	1536	1536	1526 ^f	1469 ^g
12	e_u	881	881	834	834 (47.75) ^a	822 ^f	822 ^g

^a Values in parentheses are total harmonic zero-point energies in kcal/mol. ^b Reference 48. ^c Reference 51. ^d n/a: not available. ^e Reference 52. ^f Reference 53. ^g Reference 54. ^h Reference 55.

the HF and MP2 levels for both the cc-pVTZ and adj2-cc-pVTZ basis sets are listed in Table 4. Since the adjustment to the cc-pVTZ basis affected only the oxygen basis functions, calculated geometries and vibrational frequencies for C_2H_5 and C_2H_6 species with the cc-pVTZ basis set are the same as the ones calculated with the adj2-cc-pVTZ basis set. Moreover, Table 4 lists some experimental^{48,51-55} values. It is worthwhile to note that the calculated frequencies are harmonic values, and the differences

TABLE 5: Optimized Staggered (C_2) Transition-State Structures at the HF/adj2-cc-pVTZ and MP2/adj2-cc-pVTZ Levels, respectively (bond lengths in Å, bond and dihedral angles in degrees)


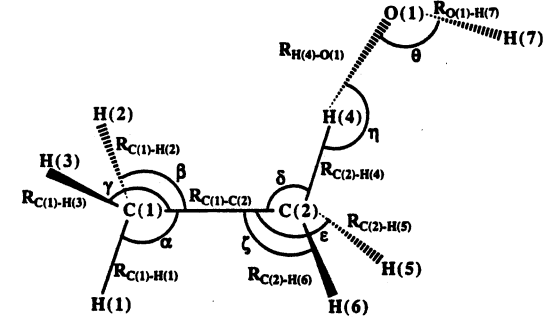
level/basis set, transition-state order	HF/adj2-cc-pVTZ, first ^a	MP2/adj2-cc-pVTZ, second ^b
$R_{C(1)-C(2)}$	1.5110	1.508
$R_{C(1)-H(1)}$	1.0862	1.0866
$R_{C(1)-H(3)}$	1.0825	1.0841
$R_{C(2)-H(4)}$	1.2785	1.1670
$R_{C(2)-H(5)}$	1.0801	1.0834
$R_{H(4)-O(1)}$	1.2349	1.3601
$R_{O(1)-H(7)}$	0.9472	0.9675
α	110.51	110.65
β	111.11	111.01
γ	106.25	107.01
δ	114.59	113.45
ϵ	178.91	175.42
ζ	99.03	95.90
η	119.77	119.87
ϕ	180.00	180.00
χ	114.65	116.51
ψ	180.00	180.00
ω	0.00	0.00

^a Saddle point. ^b Hill top. ^c τ is the dihedral angle between the H(2)-C(1)-C(2) and C(1)-C(2)-H(1) planes. ^d ϕ is the dihedral angle between the H(4)-C(2)-C(1) and C(2)-C(1)-H(1) planes. ^e χ is the dihedral angle between the H(5)-C(2)-C(1) and C(2)-C(1)-H(4) planes. ^f ψ is the dihedral angle between the O(1)-H(4)-C(2) and H(4)-C(2)-C(1) planes. ^g ω is the dihedral angle between the H(7)-O(1)-H(4) and O(1)-H(4)-C(2) planes.

between experimental harmonic and fundamental frequencies may be as large as the differences between calculated and fundamental frequencies in Table 4. Harmonic frequencies have been estimated from experiment only for 16 out of 31 cases; the available harmonic frequencies are given in Table 4 as well, and the calculated frequencies are in much better agreement with these harmonic values than with the fundamentals. Discrepancies between calculated and experimental harmonic frequencies are largest for the bond-stretching modes. Notice that, in all stable species for which harmonic frequencies are available in Table 4, using the adj2-cc-pVTZ basis at the MP2 level usually improves the frequencies as compared to using the cc-pVTZ basis, with the largest error in the former case relative to the available experimental harmonic values equal to 79 cm⁻¹, whereas in the latter case, the largest error is 102 cm⁻¹. In general, the good agreement of the MP2/adj2-cc-pVTZ frequencies in Table 4 with the available experimental harmonic values provides confidence that this is a reasonable level for studying the transition-state region.

The optimized transition-state structures calculated for the OH + C_2H_6 reaction at both the HF and MP2 levels using the adj2-cc-pVTZ basis set are given in Tables 5 and 6, respectively. As mentioned above, the transition state was located under the assumption of C_1 symmetry, resulting in a C_2 structure at the HF level and in a C_1 one at the MP2 level. The calculated Hessian matrix for these structures was found to possess only one imaginary eigenvalue, confirming that the transition-state geometry is

TABLE 6: Optimized Eclipsed (C_i) Transition-State Structure and Geometry of the Nonstationary Point along the OH + C₂H₆ Reaction Path on the Product Side of the Saddle Point at the MP2/adj2-cc-pVTZ Level (bond lengths in Å, bond and dihedral angles in degrees)



$s(a_0)$	saddle point 0.000	nonstationary point 0.005
$R_{C(1)-C(2)}$	1.5075	1.5075
$R_{C(1)-H(1)}$	1.0866	1.0871
$R_{C(1)-H(2)}$	1.0841	1.0839
$R_{C(1)-H(3)}$	1.0841	1.0843
$R_{C(2)-H(4)}$	1.1678	1.1681
$R_{C(2)-H(5)}$	1.0835	1.0843
$R_{C(2)-H(6)}$	1.0836	1.0823
$R_{H(4)-O(1)}$	1.3595	1.3581
$R_{O(1)-H(7)}$	0.9673	0.9683
α	110.71	110.72
β	110.99	111.00
γ	111.01	111.00
δ	107.65	107.60
ϵ	113.34	113.30
ζ	113.79	113.82
η	171.65	172.33
θ	96.10	95.87
τ_1^a	119.94	119.96
τ_2^b	119.90	119.89
ϕ^c	179.32	179.69
χ_1^d	117.72	117.32
χ_2^e	115.46	115.91
ψ^f	98.76	100.14
ω^g	32.21	30.64

^a τ_1 is the dihedral angle between the H(2)-C(1)-C(2) and C(1)-C(2)-H(1) planes. ^b τ_2 is the dihedral angle between the H(1)-C(2)-C(1) and C(2)-C(1)-H(3) planes. ^c ϕ is the dihedral angle between the H(4)-C(2)-C(1) and C(2)-C(1)-H(1) planes. ^d χ_1 is the dihedral angle between the H(5)-C(2)-C(1) and C(2)-C(1)-H(4) planes. ^e χ_2 is the dihedral angle between the H(4)-C(1)-C(2) and C(1)-C(2)-H(6) planes. ^f ψ is the dihedral angle between the O(1)-H(4)-C(2) and H(4)-C(2)-C(1) planes. ^g ω is the dihedral angle between the H(7)-O(1)-H(4) and O(1)-H(4)-C(2) planes.

staggered at the HF level (i.e., the O(1)-H(7) fragment is *trans* with respect to the C(1)-C(2) bond), whereas the MP2 transition-state structure is eclipsed (i.e., the O(1)-H(7) fragment is *cis* with respect to the C(2)-H(5) bond). Additionally, we computed the energy and the geometry of the staggered C_i stationary point at the MP2/adj2-cc-pVTZ level, which corresponds to the local maximum along the internal-rotation motion of the saddle point of reaction (R1). The optimized structure for the staggered transition state at the MP2/adj2-cc-pVTZ level is given in Table 5, and the energy of this structure is discussed at the end of this section.

At the HF/adj2-cc-pVTZ level (Table 5), the breaking C(2)-H(4) bond length ($R_{C(2)-H(4)}$) of the transition state is stretched by 18% compared to that in C₂H₆, whereas the making O(1)-H(4) bond (with length $R_{O(1)-H(4)}$) is elongated by 31% compared to that in H₂O, and the C(2)-H(4)-O(1) bond angle, ϵ , involving these bonds is 179°. At both the HF and MP2 levels, the transition-state structure is more reactant-like than product-like, but the extent of asymmetry changes dramatically when electron correlation is included. In particular, at the MP2/adj2-cc-pVTZ

TABLE 7: Transition-State Harmonic Vibrational Frequencies (cm⁻¹) and Harmonic Zero-Point Energies (kcal/mol)

HF/adj-cc-pVTZ	a'	4089, 3212, 3203, 3150, 1611, 1586, 1539, 1524, 1321, 1117, 1014, 786, 523, 149, 3058i
	a''	3277, 3229, 1604, 1349, 1272, 884, 466, 185, 32
	ZPE	53.07
MP2/adj-cc-pVTZ	a	3803, 3206, 3178, 3165, 3134, 3096, 1528, 1520, 1504, 1462, 1422, 1342, 1251, 1208, 1063, 1008, 880, 823, 740, 401, 166, 120, 41, 1409i
	ZPE	51.55

level (Table 6), the C(2)-H(4) bond length ($R_{C(2)-H(4)}$) is stretched by only 8% compared to the C-H bond length of C₂H₆ and the O(1)-H(4) bond (with length $R_{O(1)-H(4)}$) is 42% longer than that of H₂O. In addition, the C(2)-H(4)-O(1) bond angle at the transferred H deviates by 8° from linearity. The MP2/adj2-cc-pVTZ transition-state imaginary frequency eigenvector is primarily (more than 86% in mass-scaled coordinates) a motion of the hydrogen atom transferring between the C(2) and O(1) centers.

Table 7 lists the transition-state frequencies for reaction (R1), calculated at both the HF and MP2 levels with the adj2-cc-pVTZ basis set. The magnitude of the transition-state imaginary frequency at the HF level is 2.2 times larger than that at the MP2 level. As found earlier,⁵⁶ HF results tend to overestimate the frequencies for the bound modes at the transition state as compared to the MP2 results. This is especially true for the bond-stretching modes, with the largest error relative to the MP2 values equal to 286 cm⁻¹. Since the imaginary frequency governs the width of the classical potential energy barrier along the MEP, it plays an important role in the tunneling calculations, especially when the imaginary frequency is large, and the associated eigenvector has a large component of hydrogenic motion. Although the correlated calculation yields a much lower imaginary frequency than the Hartree-Fock calculation, the magnitude of this frequency is still quite large, 1409i cm⁻¹, which immediately indicates that tunneling is important at ambient temperatures for the OH + C₂H₆ reaction. (Quantitative calculations of the tunneling contribution are presented below.)

The above comparisons, in particular the fact that the HF calculation predicts a staggered transition-state geometry whereas the MP2 level yields an eclipsed one and the quantitative difference in bond lengths and real and imaginary frequencies, show the importance of electron correlation in predicting the potential energy surface accurately in the transition-state region.

The lowest-frequency a mode of the saddle point is 41 cm⁻¹ at the MP2 level, and it corresponds to a large-amplitude rotation of the ethyl group around the reactive C(2)-H(4) bond. The small magnitude of the frequency indicates that at the transition state, the ethyl group has a very small barrier to overcome for internal motion. Understanding the energetics of this internal motion is essential for dynamics calculations; if the barrier to internal rotation is too small, the harmonic approximation is invalid for calculating the vibrational partition functions. Consequently, we calculated the internal-rotation barrier by optimizing the C_i and C_s stationary points at three different levels of theory. We calculated the internal-rotation barrier to be 0.019, 0.019, and 0.017 kcal/mol at the MP2/adj2-cc-pVTZ, MP-SAC2//MP2/adj2-cc-pVTZ, and PMP2//MP2/adj2-cc-pVTZ levels, respectively, and we conclude that the transition state behaves as a nearly free internal rotor.

4. Stationary Point Energetics

As explained in the original paper³⁶ and elsewhere,²⁸ the SAC method corrects the treatment of electron correlation as accounted for at the MP2 level with a finite basis set by the scaling factor \mathcal{F}_2 of eq 1. The calculation of this factor is done by use of the accurate MP2 and SCF binding energies for each bond type in

TABLE 8: Theoretical Bond Dissociation Energies (kcal/mol) and \mathcal{F}_2 Parameters for MP-SAC2 Calculations

level/basis set	H-OH	fsc ₂	C-H	\mathcal{F}_2
HF/cc-pVTZ	86.53		82.87	
HF/adj2-cc-pVTZ	86.49		82.87	
MP2/cc-pVTZ	126.24	1.021	108.36	1.009
MP2/adj2-cc-pVTZ	125.78	1.009	108.36	1.009
experimental	125.44 ^a		108.14 ^b	

^a References 48, 57, and 58. ^b References 52, 54, 55, 58, and 59. These experimental values have the zero-point energy removed so that they correspond to the Born-Oppenheimer energy differences.

eq 1. Table 8 lists the calculated and experimental^{48,52,54,55,57-59} bond dissociation energies for the O-H and C-H bonds and the associated computed scaling factors \mathcal{F}_2 . The difference between the scaling factor \mathcal{F}_2 for the forming and breaking bonds gives an indication of how well balanced a basis set is for a given reaction at the MP2 level, i.e., if the difference is small, the basis set is well balanced for that reaction at the MP2 level. In the case of reaction (R1) using the large cc-pVTZ basis set, the scaling factor \mathcal{F}_2 for the O-H bond is 1.021 and that for the C-H bond is 1.009, as listed in Table 8. Since we want to use a basis set that treats electron correlation in the forming O-H bond and the breaking C-H one on an equal footing, we decided to adjust the oxygen basis functions of the cc-pVTZ basis to make a new basis set—called adj2-cc-pVTZ—that has the scaling factor \mathcal{F}_2 equal to 1.009 for both the O-H and C-H bonds of reaction (R1). We preferred to adjust the oxygen basis functions of the cc-pVTZ basis set only because adjusting the basis functions of carbon and/or hydrogen would be computationally more complicated (we preferred to recalculate the energies, geometries, and frequencies for OH and H₂O rather than for C₂H₅ and C₂H₆).

Only one cc-pVTZ oxygen basis function was adjusted, and it was changed only in its Gaussian exponential parameter, i.e., no changes were applied to the degree of contraction, the contraction coefficient, and the scale factor of the modified basis function. In particular, in order to make the adj2-cc-pVTZ basis set, the Gaussian exponential parameter to the cc-pVTZ oxygen f shell basis function was modified. For the modified oxygen f shell basis function, the cc-pVTZ Gaussian exponential parameter was decreased by a factor of 2.3 (from 1.428 to 0.60922) to make the adj2-cc-pVTZ basis set have a scaling factor \mathcal{F}_2 for the water O-H bond equal to 1.009. The absolute energy increase from a single-point HF/cc-pVTZ energy calculation to an HF/adj2-cc-pVTZ one (with both calculations at the experimental^{48,49} geometry) is 0.118 and 0.119 kcal/mol for the OH and H₂O species, respectively. However, at the MP2 level, the absolute energy increases 4.436 and 4.908 kcal/mol for OH and H₂O, respectively, whereas at the PMP2//MP2 level, the absolute energy increase is 4.441 kcal/mol for OH. (In all cases, the difference quoted is from a single-point cc-pVTZ calculation to an adj2-cc-pVTZ one at the experimental geometry.) For completeness, we note that these energy differences for OH and H₂O between the cc-pVTZ and adj2-cc-pVTZ basis sets are less than 1 mhartree at the HF level and 7-8 mhartrees at the MP2 level. At the PMP2//MP2 level, the energy difference for OH between the cc-pVTZ and adj2-cc-pVTZ basis sets is 7 mhartrees.

It should be emphasized that the "correlation balance" achieved by the present adjustment is concerned with balance between the O-H and C-H bonds and not with other kinds of balance, e.g.,

that between s, p, d, and f shells. A similar balance could have been obtained by altering other basis function parameters, but the present approach was adopted because of its simplicity.

Table 9 lists the forward and reverse classical barrier heights at different levels of theory calculated with the adj2-cc-pVTZ basis set. At the HF/adj2-cc-pVTZ level, the forward and reverse barriers are predicted to be on the order of 26-30 kcal/mol. However, including electron correlation at the MP2/adj2-cc-pVTZ level dramatically lowers the HF forward barrier by more than a factor of 4.4 while it decreases the HF reverse barrier by 23%. Single-point MP-SAC2 calculations using MP2/adj2-cc-pVTZ optimized structures, denoted as MP-SAC2//MP2/adj2-cc-pVTZ, increase the MP2 forward barrier by 0.13 kcal/mol and the reverse one by 0.01 kcal/mol, since the \mathcal{F}_2 scaling factor is slightly higher than unity, namely 1.009.

Single-point calculations were also carried out by the PMP2 method at the MP2/adj2-cc-pVTZ optimized geometries for OH, C₂H₅, and the saddle point. These PMP2//MP2/adj2-cc-pVTZ calculations give the best prediction for these barriers; they yield a classical forward barrier of 3.99 kcal/mol and a classical reverse barrier of 21.63 kcal/mol. Including the harmonic zero-point energy contribution calculated at the MP2/adj2-cc-pVTZ level lowers the effective forward barrier to 2.33 kcal/mol and the effective reverse one to 21.58 kcal/mol at the conventional transition-state theory level.

The geometry of the nonstationary point along the OH + C₂H₆ reaction path on the product side of the saddle point at the MP2/adj2-cc-pVTZ level was determined by taking a step of length 0.005 a₀ in the direction of the mass-scaled eigenvector corresponding to the saddle point imaginary frequency, and it is listed in Table 6. A PMP2//MP2/adj2-cc-pVTZ energy was also calculated for this point at $s = 0.005$ a₀. (See the supplementary material for absolute energies.) At the nonstationary point, the breaking C(2)-H(4) bond length ($R_{C(2)-H(4)}$) is elongated by 0.0003 Å, and the making O(1)-H(4) bond (with length $R_{O(1)-H(4)}$) is shortened by 0.0014 Å compared to in the saddle point geometry.

We will base our kinetic calculations for the OH + C₂H₆ reaction on the PMP2//MP2/adj2-cc-pVTZ energies instead of the MP2/adj2-cc-pVTZ or MP-SAC2//MP2/adj2-cc-pVTZ ones since the projected calculations show an appreciable correction for spin contamination. The PMP2 calculations remove this contamination for the present case without introducing a large error in the reaction's exoergicity value. In particular, the PMP2//MP2 exoergicity, although not explicitly forced to come out right as in the SAC calculations, is very close to the experimental one (Table 9). For comparison purposes, we list in Table 10 the MP2/cc-pVTZ and PMP2//MP2/cc-pVTZ forward and reverse classical barrier heights and their respective exoergicity values for the OH + CH₄ reaction (the PMP2//MP2 level of theory was not considered in ref 28). Although we notice that the PMP2//MP2/cc-pVTZ forward classical barrier height for OH + CH₄ is lowered by 1.04 kcal/mol compared to the MP-SAC2//MP2/adj2-cc-pVTZ value,²⁸ the PMP2//MP2/cc-pVTZ reaction's exoergicity is overestimated by 1.78 kcal/mol compared to the experimental value. This exoergicity overestimation makes us believe that for OH + CH₄ the MP-SAC2//MP2/adj2-cc-pVTZ energy calculations are more appropriate for dynamical studies than the PMP2//MP2/cc-pVTZ ones; we will use the PMP2//MP2/adj2-cc-pVTZ calculations for OH + C₂H₆.

TABLE 9: Classical Barrier Heights and Their Difference (kcal/mol) Calculated with the adj2-cc-pVTZ Basis Set for the OH + C₂H₆ → H₂O + C₂H₅ Reaction

quantity	HF	MP2	MP-SAC2//MP2	PMP2	experimental
forward barrier	25.96	5.79 (4.14) ^a	5.92 (4.27) ^a	3.99 (2.33) ^a	
reverse barrier	29.97	23.21 (23.16) ^a	23.22 (23.17) ^a	21.63 (21.58) ^a	
difference	4.01	17.42 (19.02) ^a	17.30 (18.90) ^a	17.64 (19.24) ^a	17.30 ^b

^a Values in parentheses are the zero-point energy corrected barriers at the saddle point. ^b By subtracting bond energies in Table 8.

TABLE 10: Classical Barrier Heights and Their Difference (kcal/mol) for the OH + CH₄ → H₂O + CH₃ Reaction

quantity	MP2/ cc-pVTZ	PMP2//MP2/ cc-pVTZ	experimental
forward barrier	8.38	6.33	
reverse barrier	23.33	21.39	
difference	14.96	15.05	13.27 ^a

^a Reference 48.

In the following sections, we briefly review the interpolated variational transition-state theory scheme and we discuss the dynamical results based on using the above *ab initio* results to calculate the rate constant including tunneling for the OH + C₂H₆ reaction. Furthermore, we compare to the best available experimental data in order to check the accuracy of our *ab initio* calculations.

5. Interpolated Variational Transition-State Theory

An extensive discussion of various models for interpolated variational transition-state theory—including the one employed for the current study—has been presented in a paper by Gonzalez-Lafont et al.²⁷ Here, we briefly summarize the approximations employed for the present calculations, and we refer readers to the above study and to previous discussions of generalized transition-state theory and semiclassical tunneling methods for a complete review of the dynamical theory^{26,27,30,31,46} and its validation.^{27,60}

The VTST rate constant to be considered in this study is given by^{26,32,46}

$$k^{\text{CVT/G}}(T) = \kappa^{\text{CVT/G}}(T) k^{\text{CVT}}(T) \quad (3)$$

where T is the temperature, $\kappa^{\text{CVT/G}}(T)$ is a ground-state (G) transmission coefficient which accounts for tunneling along the reaction coordinate, and $k^{\text{CVT}}(T)$ is the “hybrid” canonical variational transition-state theory (CVT) rate constant, for which bound vibrations are quantized (not only at the saddle point and reactants but also along the reaction path) but motion along the reaction coordinate is classical. The hybrid theoretical rate coefficient $k^{\text{CVT}}(T)$ can be obtained by variationally minimizing the generalized transition-state theory rate constant $k^{\text{GT}}(T, s)$ with respect to the positions s of the generalized transition state along the reaction coordinate,

$$k^{\text{CVT}}(T) = \min_s k^{\text{GT}}(T, s) \quad (4)$$

where

$$k^{\text{GT}}(T, s) = \frac{\sigma}{\beta h} \frac{Q^{\text{GT}}(T, s)}{\Phi^{\text{R}}(T)} e^{-\beta V_{\text{MEP}}(s)} \quad (5)$$

In eq 5, s is the distance of the generalized transition state along the MEP (we always define the origin of the reaction coordinate, $s = 0$, at the saddle point), σ is the symmetry factor⁶¹ accounting for the possibility of two or more symmetry-related reaction paths, β is $(kT)^{-1}$, k is Boltzmann's constant, h is Planck's constant, $\Phi^{\text{R}}(T)$ is the reactant partition function per unit volume excluding symmetry numbers for rotation, $V_{\text{MEP}}(s)$ is the classical energy (also called the Born–Oppenheimer potential) along the MEP with its overall zero of energy at the reactant, and $Q^{\text{GT}}(T, s)$ is the partition function of the generalized transition state at s with the local zero of energy at $V_{\text{MEP}}(s)$ and with all rotational symmetry numbers set to unity.

As just mentioned, all symmetry numbers are excluded from rotational partition functions, which are treated by classical mechanics, and we include them in σ . Then, the symmetry factor for reaction (R1) is given by

$$\sigma = \frac{\sigma_{\text{C}_2\text{H}_6} \sigma_{\text{OH}}}{\sigma_{\text{GT}}} \quad (6)$$

where σ_{GT} , $\sigma_{\text{C}_2\text{H}_6}$, and σ_{OH} are the symmetry numbers for the generalized transition state, C₂H₆, and OH, respectively. σ_{GT}

and σ_{OH} are equal to 1, whereas $\sigma_{\text{C}_2\text{H}_6}$ is equal to 6. Thus, a symmetry factor σ equal to 6 is obtained from eq 6 for the reaction OH + C₂H₆.

All partition functions in eq 5 are approximated as products of translational, rotational, vibrational, and electronic partition functions. The only structural information required to calculate the rotational partition function is the product, denoted P , of the three principal moments of inertia, which can be calculated straightforwardly from the geometry.

The harmonic approximation is assumed for the calculation of the vibrational partition function in all cases, except for the internal-rotational motion of the ethyl group around the reactive O(2)–H(4) bond at the transition state and along the MEP where a hindered rotor^{28,31,62} model has been employed. A brief discussion of the hindered rotor model is given below. The total vibrational information required is the set of all harmonic frequencies as a function of s , the symmetry number σ_{ir} for internal rotation, and the moment of inertia I_{r} for the internal rotation (also called the reduced moment of inertia).

The partition function for a hindered rotor is approximated as^{28,31,62}

$$Q^{\text{hin}} = Q^{\text{har}} f \quad (7)$$

where Q^{har} is the harmonic partition function at temperature T ,

$$Q^{\text{har}} = 0.5 \text{csch}(0.5u) \quad (8)$$

u is given by

$$u = \frac{\hbar \omega}{kT} \quad (9)$$

\hbar is Dirac's \hbar , ω is the frequency, k is Boltzmann's constant, and f is an interpolating function⁶² between the harmonic vibration approximation and the free classical rotor model^{63,64} expressed as

$$f = \tanh(Q^{\text{fr}} u) \quad (10)$$

where Q^{fr} is the free rotor partition function at temperature T

$$Q^{\text{fr}} = (\sigma_{\text{ir}} \hbar)^{-1} (2\pi I_{\text{r}} kT)^{1/2} \quad (11)$$

For reaction (R1), σ_{ir} is equal to 3 and I_{r} is equal to 111 513 au at the saddle point.

We assume that the electronic excitation energies and degeneracies of the generalized transition state are the same as the conventional transition-state ones. In particular, for the reaction OH + C₂H₆, we assume no low-lying excited states of the ²A saddle point but we correctly include the ²Π_{1/2} excited state of OH in the reactant partition function. The excitation energy of this state of OH is 140 cm^{−1}.⁴⁸

Since we use the harmonic approximation for all modes except the internal rotation and our treatment of the internal rotation is equivalent to the harmonic approximation at 0 K,^{28,31,62} the vibrationally adiabatic ground-state potential energy curve is expressed (for nonlinear generalized transition states) as

$$V_{\text{a}}^{\text{G}}(s) = V_{\text{MEP}}(s) + \frac{1}{2} \hbar c \sum_{m=1}^{3N-7} \bar{\nu}_m(s) \quad (12)$$

where c is the speed of light and $\bar{\nu}_m$ is a generalized normal-mode frequency^{26,65,66} in wave numbers. The maximum of the $V_{\text{a}}^{\text{G}}(s)$ curve and its location are denoted as V_{a}^{AG} and s^{AG} , respectively.

Since tunneling calculations are sensitive to $V_{\text{a}}^{\text{G}}(s)$ over a wider range of the reaction coordinate than the CVT calculation requires, in the ZCT^{24,26,31,32} approximation the evaluation of the transmission coefficient $\kappa^{\text{CVT/G}}(T)$ requires, in addition to the information needed for the $k^{\text{CVT}}(T)$ calculation, the generalized vibrational frequencies $\bar{\nu}_m(s)$ over a wider range of s .

One additional quantity, the effective reduced mass^{30,31,67} $\mu_{\text{eff}}(s)$, is required in the SCT^{30,31} approximation. The effective reduced mass is a function of the reaction path curvature^{26,66,68} components $\kappa_m(s)$, the ground-state generalized normal-mode turning points $t_m(s)$, and their derivatives dt_m/ds , where all these quantities can be calculated from a knowledge of the Hessian matrix along the reaction coordinate. In the zero-curvature approximation, where reaction path curvature is neglected and tunneling is assumed to occur along the MEP, the effective reduced mass is set equal to the constant reduced mass μ of the mass-scaled coordinate system.

Rate constants are calculated by the first-order global version of interpolated variational transition-state theory²⁷ with three different transmission coefficients. First order means that *ab initio* calculations are available not only at the reactants, saddle points, and products but also at one extra point, $s = s_1$, on the reaction path near the saddle point. In our case, s_1 lies on the product side of the saddle point. The quantities interpolated from information (geometries, energies, and frequencies) about these *ab initio* points in the first-order global interpolation algorithm are the classical energy along the reaction coordinate V_{MEP} , the moment of inertia product P , the reduced moment of inertia for internal rotation I_r , the vibrational frequencies $\bar{\nu}_m$, and the effective reduced mass for tunneling μ_{eff} . The procedures for interpolating all these quantities were presented previously.^{27,28} Subsequently, V_{MEP} , P , I_r , and $\bar{\nu}_m$ are used to calculate the interpolated canonical variational transition-state rate constant k^{CVT} ; these same quantities are used to calculate the ZCT transmission coefficient, while these and μ_{eff} are used to calculate the SCT transmission coefficient.

For comparison reasons, we note that for the OH + CH₄ reaction the interpolated canonical variational transition-state rate constants k^{CVT} calculated by the first-order global version of interpolated variational transition-state theory (one extra point at $s = 0.005$) agree always within 1% with the k^{CVT} rate constants calculated by the second-order global version of interpolated variational transition-state theory (two extra points at $s = \pm 0.005$) at any temperature. However, the interpolated canonical variational transition-state theory rate constants with small-curvature tunneling $k^{\text{CVT/SCT}}$ calculated for OH + CH₄ by the first-order global version of interpolated variational transition-state theory at 250 and 800 K are 12% and 2% higher, respectively, than the $k^{\text{CVT/SCT}}$ rate constants calculated by the second-order global version of interpolated variational transition-state theory. Since 12% errors are probably small compared to errors introduced by the level of the electronic structure calculations or the use of interpolated VTST instead of semiglobal fitting, this uncertainty is acceptable, and we did not spend the extra effort required to find a nonstationary point along the OH + C₂H₆ reaction path on the reactant side of the saddle point for which physically reasonable values of the generalized normal-mode frequencies could be obtained. The reactant-side region is more difficult to treat than the product side because the potential is relatively flat in the reactant-side valley; thus, extra trials would be required on the reactant side to find a step size that provides useful information about the variation of the frequencies along the reaction path.

6. Rate Constants and Reaction Path Properties

Figure 1 shows the classical potential energy curve $V_{\text{MEP}}(s)$, and Figure 2 shows the vibrationally adiabatic ground-state potential energy curve $V_a^{\text{G}}(s)$, both with overall zero of energy at the classical equilibrium energy of reactants and both as functions of the reaction coordinate s for the OH + C₂H₆ reaction. We note that $V_{\text{MEP}}(s)$ in eq 12 was interpolated from the PMP2//MP2/adj2-cc-pVTZ calculations, while the $\bar{\nu}_m(s)$ were interpolated from the MP2/adj2-cc-pVTZ calculations. The adiabatic

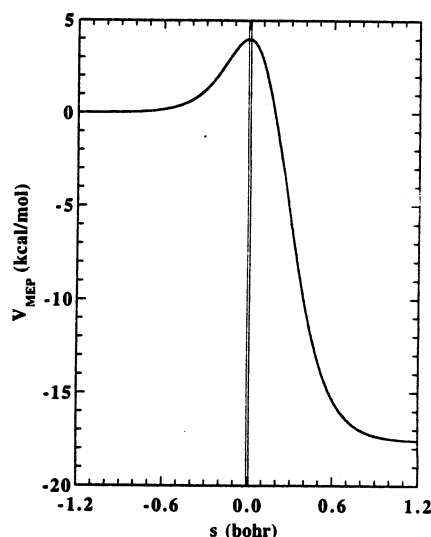


Figure 1. Potential energy along the minimum energy path as a function of reaction coordinate and with overall zero of energy at the classical equilibrium energy of reactants. The thin vertical lines show the saddle point ($s = 0$) and the location ($s = 0.005 a_0$) of the extra calculated point along the minimum energy path.

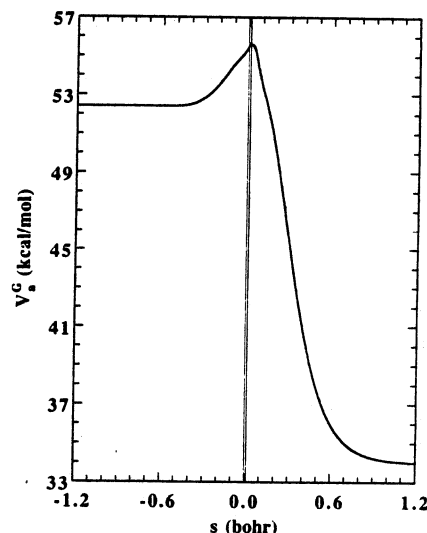


Figure 2. Vibrationally adiabatic ground-state potential energy along the minimum energy path as a function of reaction coordinate and with overall zero of energy at the classical equilibrium energy of reactants. The thin vertical lines show the saddle point ($s = 0$) and the location ($s = 0.005 a_0$) of the extra calculated point along the minimum energy path.

barrier height ΔV_a^{AG} given by

$$\Delta V_a^{\text{AG}} = V_a^{\text{AG}} - \frac{1}{2}hc \sum_{m=1}^{10} \bar{\nu}_m(s = -\infty) \quad (13)$$

is 2.453 kcal/mol, and the vibrationally adiabatic ground-state barrier occurs at $s^{\text{AG}} = 0.0065 a_0$ (Figure 2), where $V_{\text{MEP}}(s)$ is 0.004 kcal/mol lower than at the saddle point. Figures S-1 (which is in the supplementary material) and 3 show the moment of inertia product P , the reduced moment of inertia for internal rotation I_r , and the effective reduced mass μ_{eff} , respectively, along the reaction coordinate s .

The location, $s^{\text{CVT}}(T)$, of the generalized transition state ranges from 0.0072 a_0 at 200 K to 0.0096 a_0 at 3000 K. The potential energy decreases from 3.987 kcal/mol at $s = 0$ to 3.982 kcal/mol at $s = 0.0072 a_0$ and to 3.977 kcal/mol at $s = 0.0096 a_0$. Thus, at 3000 K, the variational transition state is at a location where the potential energy is 0.010 kcal/mol below its saddle point value. This illustrates the competition between potential

TABLE 11: Transition-State and Generalized Transition-State Vibrational Frequencies (cm^{-1}), Classical Energy (V_{MEP} , kcal/mol), Zero-Point Energy (ZPE, kcal/mol), and Adiabatic Ground-State Potential Energy (V_a^G , kcal/mol) along the Minimum Energy Path

	s (a_0)									
	-0.0050	0.0000	0.0050	0.0074 ^a	0.0078 ^b	0.0085 ^c	0.0100	0.0150	0.1000	1.2000
ν	3810	3803	3790	3785	3785	3785	3787	3828	3963	3963
	3203	3206	3209	3211	3211	3211	3212	3216	3362	3847
	3177	3178	3179	3179	3179	3180	3180	3181	3202	3330
	3165	3165	3164	3164	3164	3164	3165	3176	3176	3239
	3134	3134	3134	3134	3134	3134	3134	3134	3138	3168
	3099	3096	3096	3099	3100	3101	3105	3116	3127	3127
	1528	1528	1529	1530	1530	1530	1531	1533	1702	3048
	1516	1520	1523	1525	1525	1526	1527	1530	1577	1646
	1504	1504	1504	1504	1504	1504	1504	1504	1504	1520
	1464	1462	1460	1459	1459	1458	1458	1456	1416	1514
	1421	1422	1425	1427	1427	1428	1429	1434	1497	1505
	1344	1342	1339	1338	1337	1337	1336	1333	1280	1417
	1248	1251	1252	1250	1250	1249	1247	1236	1218	1218
	1206	1208	1209	1193	1189	1180	1157	1109	1098	1098
	1063	1063	1063	1063	1063	1062	1061	1047	998	998
	1006	1008	1011	1013	1013	1013	1013	998	825	825
	882	880	878	876	876	876	875	872	810	489
	826	823	819	816	816	815	813	806	199	136
	739	740	740	739	739	739	739	738	677	1
	397	401	405	407	407	407	409	412	438	1
	146	167	188	198	199	202	207	226	58	0 ^d
	100	120	142	154	155	158	165	187	32	0 ^d
	16 ^e	41 ^e	83 ^e	87 ^e	86 ^e	83 ^e	72 ^e	29 ^e	0 ^{d,e}	0 ^{d,e}
$V_{\text{MEP}}(s)$	3.984	3.987	3.984	3.981	3.981	3.980	3.977	3.965	2.862	-17.601
ZPE(s)	51.455	51.551	51.665	51.678	51.675	51.667	51.644	51.608	50.550	51.593
$V_a^G(s)$	55.440	55.537	55.649	55.659	55.656	55.647	55.621	55.574	53.412	33.993

^a s_{CVT} for 300 K. ^b s_{CVT} for 600 K. ^c s_{CVT} for 1500 K. ^d The value of this frequency is less than 0.5 cm^{-1} . ^e The hindered rotor model was assumed for this mode.

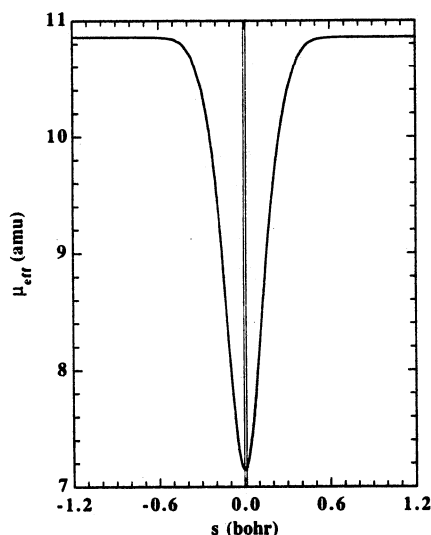


Figure 3. The effective reduced mass along the minimum energy path as a function of reaction coordinate. The thin vertical lines show the saddle point ($s = 0$) and the location ($s = 0.005 a_0$) of the extra calculated point along the minimum energy path.

energy and vibrational energy in determining the location of the variational transition state. In addition, Table 11 lists the interpolated vibrational frequencies, the classical energy, the zero-point energy, and the vibrational energy at each of several generalized transition states for three temperatures, namely 300, 600, and 1500 K. For interpretative reasons, we also include in Table 11 the vibrational frequencies, the classical energy, the zero-point energy, and the vibrational energy at the saddle point ($s = 0$) and the extra point that was calculated ($s = 0.005 a_0$), and at $s = -0.005, 0.001, 0.0150, 0.1$, and $1.2 a_0$. Table 11 clearly illustrates how the zero-point energy gradually changes along the reaction coordinate and how this change is dominated by the three low-frequency modes, namely the ones with values of 41,

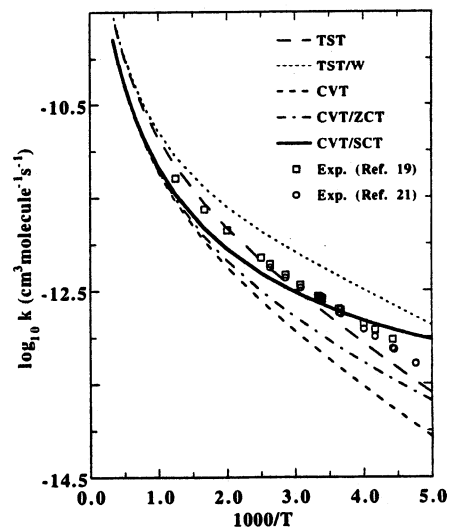


Figure 4. Plot of the logarithm of rate constants versus $1000/T$.

120, and 167 cm^{-1} at the saddle point. These three low-frequency modes—whose frequency magnitude increases by 100%, 30%, and 20%, respectively, from the saddle point to the variational transition state—are responsible for the large variational effect in the calculation of the CVT rate constants.

Tables 12, 13, and 14 list the calculated rate constants and activation energies, respectively, for the temperature range from 200 to 3000 K, and Figure 4 shows an Arrhenius plot of the various theoretical rate constants and the two recommended experimental^{19,21} rate constants, while Figure 5 shows in greater detail the logarithm of various low-temperature (210–380 K) experimental rate constant values and compares them to the CVT/SCT rate constant.

Table 12 compares the calculated rate constants to the two-temperature rate expression of ref 21 for the temperature range from 210 to 380 K and to the three-parameter rate expression

TABLE 12: Rate Constants ($\text{cm}^3 \text{molecules}^{-1} \text{s}^{-1}$) for $\text{OH} + \text{C}_2\text{H}_6 \rightarrow \text{H}_2\text{O} + \text{C}_2\text{H}_5$

T (K)	TST	TST/W	CVT	CVT/ZCT	CVT/SCT	exp ^a	exp ^b
200	2.53(-14)	1.33(-13)	8.54(-15)	2.06(-14)	9.36(-14)	n/a ^d	n/a
210	3.37(-14) ^c	1.65(-13)	1.14(-14)	2.57(-14)	1.03(-13)	n/a	5.22(-14)
225	4.97(-14)	2.18(-13)	1.70(-14)	3.46(-14)	1.19(-13)	n/a	7.42(-14)
226	5.09(-14)	2.21(-13)	1.74(-14)	3.53(-14)	1.20(-13)	9.39(-14)	7.59(-14)
240	7.01(-14)	2.78(-13)	2.40(-14)	4.54(-14)	1.37(-13)	1.19(-13)	1.01(-13)
250	8.64(-14)	3.23(-13)	2.97(-14)	5.36(-14)	1.49(-13)	1.40(-13)	1.22(-13)
270	1.26(-13)	4.22(-13)	4.37(-14)	7.28(-14)	1.78(-13)	1.87(-13)	1.69(-13)
273	1.33(-13)	4.38(-13)	4.61(-14)	7.61(-14)	1.83(-13)	1.95(-13)	1.77(-13)
275	1.38(-13)	4.49(-13)	4.78(-14)	7.83(-14)	1.86(-13)	2.00(-13)	1.82(-13)
295	1.90(-13)	5.64(-13)	6.76(-14)	1.04(-13)	2.24(-13)	2.58(-13)	2.40(-13)
297	1.96(-13)	5.76(-13)	6.97(-14)	1.07(-13)	2.27(-13)	2.64(-13)	2.46(-13)
298	1.99(-13)	5.82(-13)	7.08(-14)	1.08(-13)	2.29(-13)	2.68(-13)	2.49(-13)
300	2.05(-13)	5.95(-13)	7.30(-14)	1.11(-13)	2.33(-13)	2.74(-13)	2.55(-13)
325	2.90(-13)	7.60(-13)	1.04(-13)	1.49(-13)	2.83(-13)	3.62(-13)	3.40(-13)
350	3.94(-13)	9.45(-13)	1.43(-13)	1.95(-13)	3.42(-13)	4.65(-13)	4.34(-13)
380	5.46(-13)	1.19(-12)	2.00(-13)	2.61(-13)	4.22(-13)	6.08(-13)	5.57(-13)
400	6.65(-13)	1.38(-12)	2.45(-13)	3.12(-13)	4.83(-13)	7.16(-13)	n/a
500	1.49(-12)	2.51(-12)	5.68(-13)	6.65(-13)	8.86(-13)	1.41(-12)	n/a
550	2.07(-12)	3.24(-12)	7.99(-13)	9.11(-13)	1.16(-12)	1.85(-12)	n/a
600	2.76(-12)	4.08(-12)	1.08(-12)	1.21(-12)	1.48(-12)	2.37(-12)	n/a
800	6.94(-12)	8.79(-12)	2.88(-12)	3.07(-12)	3.44(-12)	5.10(-12)	n/a
1000	1.38(-11)	1.61(-11)	5.99(-12)	6.23(-12)	6.72(-12)	n/a	n/a
1250	2.68(-11)	2.97(-11)	1.22(-11)	1.25(-11)	1.31(-11)	n/a	n/a
1500	4.54(-11)	4.88(-11)	2.15(-11)	2.19(-11)	2.26(-11)	n/a	n/a
1750	7.02(-11)	7.41(-11)	3.42(-11)	3.47(-11)	3.56(-11)	n/a	n/a
1800	7.59(-11)	7.99(-11)	3.72(-11)	3.77(-11)	3.86(-11)	n/a	n/a
2000	1.02(-10)	1.06(-10)	5.08(-11)	5.13(-11)	5.23(-11)	n/a	n/a
2400	1.66(-10)	1.71(-10)	8.57(-11)	8.63(-11)	8.74(-11)	n/a	n/a
3000	2.97(-10)	3.03(-10)	1.59(-10)	1.59(-10)	1.61(-10)	n/a	n/a

^a Recommended values from ref 19. ^b Recommended values from ref 21. ^c Power of 10 in parentheses. ^d n/a: not available.

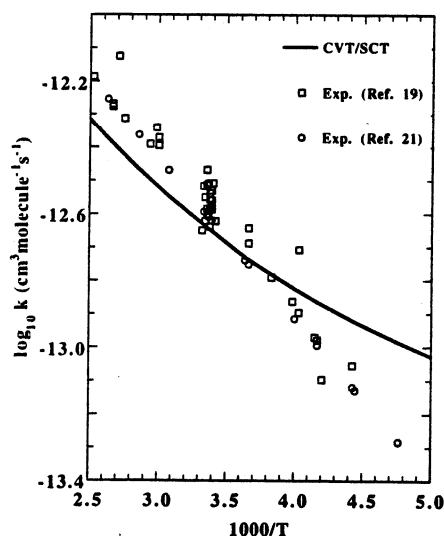


Figure 5. Plot of the logarithm of low-temperature (210–400 K) experimental rate constant values,^{19,21} compared to the logarithm of the CVT/SCT rate constant for the same temperature range, versus $1000/T$. The squares are experimental rate constant values from Greiner,² Overend et al.,³ Howard and Evenson,⁴ Leu,⁵ Margitan and Watson,⁶ Tully et al.,⁷ Jeong et al.,⁸ Smith et al.,⁹ Devolder et al.,¹⁰ Baulch et al.,¹¹ Tully et al.,¹² Stachnik et al.,¹³ Bourmada et al.,¹⁶ Wallington et al.,¹⁷ and Zabarnick et al.¹⁸ used in the evaluation of the recommended three-parameter rate expression of Atkinson.¹⁹ The circles are rate constant evaluations of the recommended two-parameter expression of Talukdar et al.,²¹ since experimental rate constant values are not available.

of ref 19 for the temperature range from 226 to 800 K. Error limits are available only for the recommended three-parameter¹⁹ rate expression, and they are approximately 20% at the level of two least-squares standard deviations. According to Table 12, the conventional transition-state theory rate constants without tunneling k^{TST} underestimate the lowest experimental rate²¹ by 35% and 20% at $T = 210$ and 300 K, respectively. The Wigner transmission coefficient⁶⁹ increases the rate constant by factors of 4.9 and 2.9 at these temperatures, i.e., it overestimates by

factors of 3.2 and 2.3 the transmission coefficient that would be required to bring theory and experiment into agreement at the temperatures $T = 210$ and 300 K, respectively. The interpolated canonical variational transition-state theory rate constants k^{CVT} are lower than the conventional transition-state theory rate constants by at least a factor of 2 for temperatures up to 2000 K. However, the interpolated canonical variational transition-state theory rate constants with zero-curvature tunneling $k^{\text{CVT/ZCT}}$ and with small-curvature tunneling $k^{\text{CVT/SCT}}$ predict rate constants which agree with experiment within a factor of 2.3 for the whole range of temperatures. In particular, the $k^{\text{CVT/ZCT}}$ rate constants always agree with the lowest recommended experimental rate within a factor of 2.3, although they systematically underestimate the experimental rate constants for the whole temperature range, for example, by 53% at 500 K. On the other hand, the $k^{\text{CVT/SCT}}$ rate constants always agree with experiment within a factor of 2.0; they underestimate the lowest experimental rate constants for a temperature range of 295 to 800 K, for example, by 38% at 600 K. In general, the very good agreement of theory with experiment confirms the validity of our *ab initio* calculations.

A critical issue in reaction rate calculations is the quantitative nature of hindered rotor corrections. First of all, we note that the transition state of this reaction actually has two hindered rotors, the internal rotation of the ethyl group around the reactive C(2)–H(4) bond, which we do treat as a hindered rotor, and the internal rotation of the C(1)–C(2) bond, which we do not. The effect of the hindered rotation of the ethyl group around the reactive bond is shown in Table 15. This anharmonic correction becomes more important at high temperature, reaching a factor of 0.493 at 3000 K.

The C(1)–C(2) bond internal rotation was treated harmonically. The calculated frequencies of this motion for reactants, saddle point, 300 K, and 3000 K variational transition states are 343, 401, 407, and 408 cm^{-1} , respectively. A simple estimate based on eq 7 indicates that treating this mode as a hindered rotor would decrease the partition functions by about 3% at 1250 K up to 14% at 3000 K, but most of this would cancel in the rate constant. Thus, the treatment of this mode as harmonic is justified.

TABLE 13: Activation Energies (kcal/mol) for OH + C₂H₆ → H₂O + C₂H₅

	T range (K)					
	210–300	226–300	300–380	500–600	1000–1500	2000–2400
TST	2.51	2.54	2.78	3.67	7.11	11.73
TST/W	1.79	1.80	1.97	2.88	6.61	11.43
CVT	2.58	2.61	2.85	3.86	7.62	12.47
CVT/ZCT	2.04	2.09	2.42	3.58	7.48	12.40
CVT/SCT	1.13	1.21	1.69	3.07	7.24	12.26
experimental ^a		1.95	2.26	3.09		
experimental ^b	2.21	2.21	2.21			

^a Reference 19. ^b Reference 21.**TABLE 14: Additional Activation Energies (kcal/mol) for OH + C₂H₆ → H₂O + C₂H₅**

	T range (K)							
	245–255	265–275	268–278	295–305	345–355	495–505	595–605	1245–1255
TST	2.51	2.56	2.57	2.65	2.82	3.45	3.93	7.30
TST/W	1.78	1.81	1.81	1.87	2.01	2.64	3.16	6.80
CVT	2.55	2.61	2.62	2.71	2.90	3.61	4.14	7.79
CVT/ZCT	2.01	2.10	2.12	2.24	2.49	3.30	3.89	7.66
CVT/SCT	1.11	1.25	1.27	1.44	1.77	2.76	3.42	7.45
experimental ^a	1.91	1.99	2.00	2.11	2.31	2.91	3.30	
experimental ^b	2.21	2.21	2.21	2.21	2.21			

^a Reference 19. ^b Reference 21.**TABLE 15: Ratio of the Hindered Rotor Approximation/Harmonic Approximation at the TST and CVT Levels**

T (K)	TST	CVT	T (K)	TST	CVT
250	0.954	0.999	600	0.836	0.988
270	0.947	0.999	1250	0.684	0.940
273	0.946	0.999	1500	0.644	0.917
300	0.936	0.999	2400	0.540	0.825
350	0.919	0.998	3000	0.493	0.761
500	0.868	0.993			

Tables 13 and 14 report Arrhenius activation energies as a function of temperature for several two-temperature fits to the theoretical and experimental results. Each fit yields the effective phenomenological activation energy for the temperature range encompassed. Both the interpolated variational transition-state theory results including tunneling and experimental^{19,21} data predict a decrease in E_a at low temperature. In particular, the calculated decrease at 210–300 K as compared to 300–380 K is about 0.5 kcal/mol, and this agrees very well with the 0.3 kcal/mol experimental decrease. However, the overestimation of the Arrhenius curvature is clear in Figure 4. We cannot explain the larger Arrhenius curvature in the theoretical calculations as compared to experiment, but some possible explanations for the trends are that the calculated barrier is too high (which would lead to too much tunneling), that the interpolation leads to too narrow of a barrier or too large a curvature effect, or that the SCT approximation predicts too much tunneling. Future study of these issues would be of great interest.

Since low temperatures are important for atmospheric chemistry and the temperature dependence of the $k^{\text{CVT/SCT}}$ rate constant is in reasonably good agreement with experiment down to about 250 K, we emphasize the significance of the tunneling effect for 250–400 K, where more than half the reactive events are predicted to occur by tunneling. Furthermore, the predicted tunneling contribution is even larger at temperatures below 250 K, but it may be quantitatively less reliable since further work is required to understand the reliability of the tunneling calculation for very low temperatures.

Since the understanding of substituent effects is very important in both combustion and atmospheric chemistry, we next reconsider the comparison of the present calculations to those for OH + CH₄ in order to understand the effect of methyl substitution.

TABLE 16: Classical Forward Barrier Heights Calculated at Various Levels of Theory and Experimental Activation Energy at 600 K (both in kcal/mol) for the OH + CH₄ → H₂O + CH₃ and OH + C₂H₆ → H₂O + C₂H₅ Reactions

system	classical barrier height			E_a , exp
	HF/a-cc-pVTZ ^a	MP-SAC2//MP2/a-cc-pVTZ ^a	PMP2//MP2/a2-cc-pVTZ ^b	
OH + CH ₄	28.3 (26.6) ^c	7.4 (5.9) ^c	6.3 (4.9) ^c	4.9 ^d
OH + C ₂ H ₆	26.0 (24.0) ^c	5.9 (4.3) ^c	4.0 (2.3) ^c	3.3 ^e
difference	2.3 (2.6) ^c	1.5 (1.6) ^c	2.3 (2.6) ^c	1.6

^a a-cc-pVTZ denotes adj-cc-pVTZ for OH + CH₄ and adj2-cc-pVTZ for OH + C₂H₆. ^b a2-cc-pVTZ denotes cc-pVTZ for OH + CH₄ and adj2-cc-pVTZ for OH + C₂H₆. ^c Values in parentheses are the zero-point energy corrected barriers at the saddle point. ^d Reference 19. ^e Reference 68.

TABLE 17: Rate Constant Ratios' Factors of the OH + C₂H₆ Reaction to OH + CH₄ at Various Temperatures

T (K)	method	TunF	SF	TranF	RF	VF	PF	k_{C_2}/k_{C_1}
300	TST		0.50	0.66	0.39	6.96	289.5	257.2
	CVT		0.50	0.66	0.39	4.28	201.0	112.8
	CVT/SCT	0.36	0.50	0.66	0.39	4.28	201.0	41.15
600	TST		0.50	0.66	0.39	9.89	17.02	21.48
	CVT		0.50	0.66	0.39	5.58	13.92	10.21
	CVT/SCT	0.85	0.50	0.66	0.39	5.58	13.92	8.68
1250	TST		0.50	0.66	0.39	12.29	3.90	6.12
	CVT		0.50	0.66	0.39	7.19	3.50	3.31
	CVT/SCT	0.97	0.50	0.66	0.39	7.19	3.50	3.21

Table 16 lists classical forward barrier heights for the OH + CH₄ and OH + C₂H₆ reactions, calculated at various levels of theory, and their respective differences. At each level of theory, the difference between the OH + CH₄ and OH + C₂H₆ classical barrier heights—although the basis set was adjusted separately for each reaction—ranges from 1.5 to 2.3 kcal/mol, whereas the difference between the respective zero-point inclusive forward barrier heights ranges from 1.6 to 2.6 kcal/mol.

It is interesting to dissect the rate constants ratios k_{C_2}/k_{C_1} of the OH + C₂H₆ reaction to OH + CH₄—calculated using our best level of theory in each case, i.e., the PMP2//MP2/adj2-cc-pVTZ and MP-SAC2//MP2/adj-cc-pVTZ levels of theory, respectively. The ratio is factored as follows:

$$k_{C_2}(T)/k_{C_1}(T) = \left[\frac{\kappa_{C_2}(T)}{\kappa_{C_1}(T)} \right] \left[\frac{\sigma_{C_2}}{\sigma_{C_1}} \right] \left[\frac{Q^{\text{R}}_{\text{trans},C_1}(T)}{Q^{\text{R}}_{\text{trans},C_2}(T)} \right] \times \left[\frac{Q^{\text{GT}}_{\text{rot},C_2}(T,s) Q^{\text{R}}_{\text{rot},C_1}(T)}{Q^{\text{GT}}_{\text{rot},C_1}(T,s) Q^{\text{R}}_{\text{rot},C_2}(T)} \right] \times \left[\frac{Q^{\text{GT}}_{\text{vib},C_2}(T,s) Q^{\text{R}}_{\text{vib},C_1}(T)}{Q^{\text{GT}}_{\text{vib},C_1}(T,s) Q^{\text{R}}_{\text{vib},C_2}(T)} \right] \times [e^{-(V^{\text{GT}}_{\text{MEP},C_1}(s) - V^{\text{GT}}_{\text{MEP},C_2}(s))/RT}] \quad (14)$$

where the first factor is called TunF (tunneling factor), the second one SF (symmetry factor), the third one TranF (translational factor), the fourth one RF (rotational factor), the fifth one VF (vibrational factor), and the last one PF (potential factor). Table 17 lists these factors, calculated at the TST, CVT, and CVT/SCT levels, at three different temperatures, namely 300, 600, and 1250 K. Examination of Table 17 shows that at low and medium temperatures, the PF plays the dominant role on the final result, whereas at medium to high temperatures, the VF makes the largest contribution to the rate constant ratio. It is important to note, though, that both RF and VF are quantitatively significant at all temperatures.

The final CVT/SCT prediction for k_{C_2}/k_{C_1} differs from the PF contribution alone by factors of 4.9, 1.6, and 1.1 at 300, 600, and 1250 K, respectively. The latter two small ratios are

TABLE 18: Arrhenius Coefficient Ratios and Activation Energies Differences for the OH + C₂H₆ and OH + CH₄ Reactions in Three Temperature Regions

T (K)	method	$A_{C_2H_6-OH}/A_{CH_4-OH}$	$E_{a,CH_4-OH} - E_{a,C_2H_6-OH}$ (kcal/mol)
295–305	TST	1.62	3.02
	CVT	0.77	2.97
	CVT/SCT	4.79	1.28
	experimental ^a	2.04	1.63
	experimental ^b	3.53	1.43
595–605	TST	1.88	2.90
	CVT	1.04	2.73
	CVT/SCT	1.31	2.26
	experimental ^a	2.04	1.63
	experimental ^c	1.94	2.85
1245–1255	TST	1.94	2.85
	CVT	1.27	2.39
	CVT/SCT	1.32	2.20
	experimental	n/a ^c	n/a

^a Reference 19. ^b References 21 and 70. ^c n/a: not available.

accidentally close to unity because the symmetry factor cancels part of the other effects. Thus, simple theories that attempt to explain substituent effects strictly on the basis of electronic factors affecting the barrier heights cannot count quantitatively for the whole effect.

Finally, Table 18 compares Arrhenius parameters calculated by different levels of dynamical theory for the two reactions. The table shows that the CVT/SCT calculations predict $E_{a,CH_4-OH} - E_{a,C_2H_6-OH}$ values that differ from the experimental^{19,21,70} ones by about 0.15–0.6 kcal/mol, while at the TST level, $E_{a,CH_4-OH} - E_{a,C_2H_6-OH}$ values overestimate experimental values by about 1.3–1.6 kcal/mol. There are less systematic differences in the $A_{C_2H_6-OH}/A_{CH_4-OH}$ ratios.

7. Conclusions

The classical forward and reverse barrier heights for the reaction OH + C₂H₆ are predicted to be 4.0 and 21.6 kcal/mol, respectively, at the PMP2//MP2/adj2-cc-pVTZ level. Electron correlation was found to be very important, both for predicting the correct geometry of the transition state, and for calculating the vibrational frequencies. Furthermore, the adj2-cc-pVTZ basis set is correlation balanced for the forming and breaking bonds of the OH + C₂H₆ reaction so the calculations yield almost equally accurate barrier heights for both directions of reaction.

The internal-rotation barrier of the ethyl group around the reactive C(2)–H(4) bond at the saddle point is predicted to be only 0.02 kcal/mol, and the transition state behaves dynamically as an almost free internal rotor. The difference between treating this mode harmonically and as a hindered rotor is greatest at high temperature. For example, at 2400 K, the factor is 0.54.

Rate constants for the above reaction have been calculated for a temperature range of 200–3000 K. The SCT tunneling contribution increases the CVT rate constant by a factor of 5 or more at 250 K, and the transmission coefficient remains equal to 2 or more up to 400 K. It is very promising that the first-order global interpolation method predicts rate constants within a factor of 2 of experimental data. Clearly, practical *ab initio* calculations of rate constants with good accuracy are now practical even for systems with 10 atoms.

Acknowledgment. We are grateful to Richard B. Walsh for assistance with the electronic structure calculations. Vasilios S. Melissa gratefully acknowledges the support of a Rohm & Haas Fellowship during part of the course of this work. The electronic structure calculations were supported by the University of Minnesota Supercomputer Institute by providing supercomputer resources at the Minnesota Supercomputer Center and by the National Science Foundation through a grant at the San Diego Supercomputer Center. The variational transition-state theory

calculations were supported in part by the Division of Chemical Sciences, Office of Basic Energy Sciences, U.S. Department of Energy, through Grant No. DE-FG02-86ER13579.

Supplementary Material Available: Tables S-I and S-II containing the absolute energies in hartrees for all optimizations and single-point calculations, respectively, mentioned in this paper and Figure S-I showing interpolated values of the moment of inertia product and the reduced moment of inertia for internal rotation as functions of distance along the reaction coordinate (5 pages). For ordering information see any masthead page.

References and Notes

- (1) Schiffman, A.; Nelson, D. D.; Robinson, M. S.; Nesbitt, D. J. *J. Phys. Chem.* 1991, 95, 2629.
- (2) Greiner, N. R. *J. Chem. Phys.* 1970, 53, 1070.
- (3) Overend, R. P.; Paraskevopoulos, G.; Cvetanovic, R. J. *Can. J. Chem.* 1975, 53, 3374.
- (4) Howard, C. J.; Evenson, K. M. *J. Chem. Phys.* 1976, 64, 197.
- (5) Leu, M.-T. *J. Chem. Phys.* 1979, 70, 1662.
- (6) Margitan, J. J.; Watson, R. T. *J. Phys. Chem.* 1982, 86, 3819.
- (7) Tully, F. P.; Ravishankara, A. R.; Carr, K. *Int. J. Chem. Kinet.* 1983, 15, 1111.
- (8) Jeong, K.-M.; Hsu, K.-J.; Jeffries, J. B.; Kaufman, F. J. *Phys. Chem.* 1984, 88, 1222.
- (9) Smith, C. A.; Molina, L. T.; Lamb, J. J.; Molina, M. J. *Int. J. Chem. Kinet.* 1984, 16, 41.
- (10) Devolder, P.; Carlier, M.; Pauwels, J. F.; Sochet, L. R. *Chem. Phys. Lett.* 1984, 111, 94.
- (11) Baulch, D. L.; Campbell, I. M.; Saunders, S. M. *J. Chem. Soc., Faraday Trans. 1* 1985, 81, 259.
- (12) Tully, F. P.; Droge, A. T.; Koszykowski, M. L.; Melius, C. F. *J. Phys. Chem.* 1986, 90, 69.
- (13) Stachnik, R. A.; Molina, L. T.; Molina, M. J. *J. Phys. Chem.* 1986, 90, 2777.
- (14) Atkinson, R. *Chem. Rev.* 1986, 86, 69.
- (15) Baulch, D. L.; Bowers, M.; Malcolm, D. G.; Tuckerman, R. T. *J. Phys. Chem. Ref. Data* 1986, 15, 465.
- (16) Bourmada, N.; Lafage, C.; Devolder, P. *Chem. Phys. Lett.* 1987, 136, 209.
- (17) Wallington, T. J.; Neuman, D. M.; Kurylo, M. J. *Int. J. Chem. Kinet.* 1987, 19, 725.
- (18) Zabarnick, S.; Fleming, J. W.; Lin, M. C. *Int. J. Chem. Kinet.* 1988, 20, 117.
- (19) Atkinson, R. *J. Phys. Chem. Ref. Data* 1989, Monograph 1, 18.
- (20) Abbott, J. P. D.; Demerjian, K. L.; Anderson, J. G. *J. Phys. Chem.* 1990, 94, 4566.
- (21) Talukdar, R. K.; Mellouki, A.; Gierczak, T.; Barone, S.; Chiang, S.-Y.; Ravishankara, A. R. In *1991 Fall Meeting, American Geophysical Union*: San Francisco, CA, 1991; p 101.
- (22) DeMore, W. B.; Sander, S. P.; Golden, D. M.; Hampson, R. F.; Kurylo, M. J.; Howard, C. J.; Ravishankara, A. R.; Kolb, C. E.; Molina, M. J. *NASA JPL Publ.* 1992, 92–20, 47.
- (23) (a) Shavitt, I. University of Wisconsin Theoretical Chemistry Laboratory Technical Report WIS-AEC-23; Madison, WI, 1959 (unpublished). (b) Marcus, R. A. *J. Chem. Phys.* 1964, 41, 10. (c) Marcus, R. A. *Ibid.* 1966, 45, 4493. (d) Marcus, R. A. *Ibid.* 1968, 49, 2610.
- (24) (a) Truhlar, D. G.; Kuppermann, A. *J. Am. Chem. Soc.* 1971, 93, 1840. (b) Truhlar, D. G.; Kuppermann, A. *Chem. Phys. Lett.* 1971, 9, 269.
- (25) Fukui, K. In *The World of Quantum Chemistry*; Daudel, R., Pullman, B., Eds.; Reidel: Dordrecht, The Netherlands, 1974; p 113.
- (26) Truhlar, D. G.; Isaacson, A. D.; Garrett, B. C. In *Theory of Chemical Reaction Dynamics*, Baer, M., Ed.; CRC: Boca Raton, FL, 1985; Vol. IV, p 65.
- (27) Gonzalez-Lafont, A.; Truong, T. N.; Truhlar, D. G. *J. Chem. Phys.* 1991, 95, 8875.
- (28) Melissas, V. S.; Truhlar, D. G. *J. Chem. Phys.* 1993, 99, 1013.
- (29) Melissas, V. S.; Truhlar, D. G. *J. Chem. Phys.* 1993, 99, 3542.
- (30) Liu, Y.-P.; Lynch, G. C.; Truong, T. N.; Lu, D.-h.; Truhlar, D. G.; Garrett, B. C. *J. Am. Chem. Soc.* 1993, 115, 2408.
- (31) Lu, D.-h.; Truong, T. N.; Melissas, V. S.; Lynch, G. C.; Liu, Y.-P.; Garrett, B. C.; Steckler, R.; Isaacson, A. D.; Rai, S. N.; Hancock, G. C.; Lauderdale, J. G.; Joseph, T.; Truhlar, D. G. *Comp. Phys. Commun.* 1992, 71, 235.
- (32) Garrett, B. C.; Truhlar, D. G.; Grev, R. S.; Magnuson, A. W. *J. Phys. Chem.* 1984, 84, 1730; 1983, 87, 4554.
- (33) Hehre, W. J.; Radom, L.; Schleyer, P. v. R.; Pople, J. A. *Ab Initio Molecular Orbital Theory*; Wiley: New York, 1986.
- (34) (a) Sosa, C.; Schlegel, H. B. *Int. J. Quantum Chem.* 1986, 29, 1001. (b) Sosa, C.; Schlegel, H. B. *Ibid.* 1987, 30, 155.
- (35) (a) Sosa, C.; Schlegel, H. B. *Int. J. Quantum Chem. Symp.* 1987, 21, 267. (b) Gonzalez, C.; Sosa, C.; Schlegel, H. B. *J. Phys. Chem.* 1989, 93, 2435.
- (36) Gordon, M. S.; Truhlar, D. G. *J. Am. Chem. Soc.* 1986, 108, 5412.
- (37) Dunning, T. H., Jr. *J. Chem. Phys.* 1989, 90, 1007.

- (38) Schlegel, H. B. *J. Comput. Chem.* **1982**, *3*, 214.
(39) Gordon, M. S.; Pople, J. A. MBLD, Quantum Chemistry Program Exchange Program No. 135, *QCPE Newsletter* **1969**, *22*, 28.
(40) Schlegel, H. B. In *New Theoretical Concepts for Understanding Organic Reactions*; Bertrán, J., Csizmadia, I. G., Eds.; Kluwer: Dordrecht, The Netherlands, 1989; p 33.
(41) Schlegel, H. B. *Adv. Chem. Phys.* **1987**, *67*, 249.
(42) Almlöf, J.; Faegri, K., Jr.; Korsell, K. *J. Comput. Chem.* **1982**, *3*, 385.
(43) (a) Gill, P. M. W.; Head-Gordon, M.; Pople, J. A. *Int. J. Quantum Chem., Symp.* **1989**, *23*, 269. (b) Gill, P. M. W.; Head-Gordon, M.; Pople, J. A. *J. Phys. Chem.* **1990**, *94*, 5564. (c) Gill, P. M. W.; Johnson, B. G.; Pople, J. A. *Int. J. Quantum Chem.* **1991**, *40*, 745. (d) Gill, P. M. W.; Pople, J. A. *Ibid.* **1991**, *40*, 753. (e) Johnson, B. G.; Gill, P. M. W.; Pople, J. A. *Ibid.* **1991**, *40*, 809.
(44) (a) Pople, J. A.; Krishnan, R.; Schlegel, H. B.; Binkley, J. S. *Int. J. Quantum Chem., Symp.* **1979**, *13*, 225. (b) Takada, T.; Dupuis, M.; King, H. F. *J. Chem. Phys.* **1981**, *75*, 332. (c) Saxe, P.; Yamaguchi, Y.; Schaefer, H. F. *Ibid.* **1982**, *77*, 5647.
(45) Trucks, G. W.; Frisch, M. J.; Head-Gordon, M.; Andres, J.; Schlegel, H. B.; Salter, A. *J. Chem. Phys.* **1993**, accepted for publication.
(46) Isaacson, A. D.; Truhlar, D. G. *J. Chem. Phys.* **1982**, *76*, 1380.
(47) Frisch, M. J.; Trucks, G. W.; Head-Gordon, M.; Gill, P. M. W.; Wong, M. W.; Foresman, J. B.; Johnson, B. G.; Schlegel, H. B.; Robb, M. A.; Replogle, E. S.; Gomperts, R.; Andres, J. L.; Raghavachari, K.; Binkley, J. S.; Gonzalez, C.; Martin, R. L.; Fox, D. J.; Defrees, D. J.; Baker, J.; Stewart, J. J. P.; Pople, J. A. GAUSSIAN92; Gaussian, Inc.: Pittsburgh, PA, 1992.
(48) *JANAF Thermochemical Tables*, 3rd ed.; Chase, M. W., Jr., Davies, C. A., Downey, J. R., Jr., Frurip, D. J., McDonald, R. A., Syverud, A. N., Eds.; Natl. Stand. Ref. Data Ser.; Natl. Bur. Stand.: Washington, DC, 1985; Vol. 14.
(49) Benedict, W. S.; Gailar, N.; Plyler, E. K. *J. Chem. Phys.* **1956**, *24*, 1139.
(50) Harmony, M. D. *J. Chem. Phys.* **1990**, *93*, 7522.
(51) Hoy, A. R.; Mills, I. M.; Strey, G. *Mol. Phys.* **1972**, *24*, 1265.
(52) (a) Pacansky, J.; Dupuis, M. *J. Am. Chem. Soc.* **1982**, *104*, 415. (b) Pacansky, J.; Schrader, B. *J. Chem. Phys.* **1983**, *78*, 1033.
(53) (a) Hansen, G. E.; Dennison, D. M. *J. Chem. Phys.* **1952**, *20*, 313. (b) Mille, K. J.; Ganda-Kesuma, F. S. *J. Mol. Spectrosc.* **1991**, *145*, 429.
(54) *Tables of Molecular Vibrational Frequencies*; Shimanouchi, T., Ed.; Natl. Stand. Ref. Data Ser.; Natl. Bur. Stand.: Washington, DC, 1972; Vol. 1.
(55) Cole, A. R.; Cross, K. J.; Cugley, J. A.; Heise, H. M. *J. Mol. Spectrosc.* **1980**, *83*, 233.
(56) Truong, T. N.; Truhlar, D. G. *J. Chem. Phys.* **1990**, *93*, 1761; **1992**, *97*, 8820.
(57) Task Group of the Committee on Data Science and Technology of the International Council of Scientific Unions, *J. Chem. Thermodyn.* **1978**, *10*, 903.
(58) An analysis of the experimental data in order to extract these values of the Born-Oppenheimer bond dissociation energies is given in Melissas, V. S. Ph.D. Thesis, University of Minnesota, Minneapolis, MN, 1993.
(59) (a) Pamidimukkala, K. M.; Rogers, D.; Skinner, G. B. *J. Phys. Chem. Ref. Data* **1982**, *11*, 83. (b) Brouard, M.; Lightfoot, P. D.; Pilling, M. J. *J. Phys. Chem.* **1986**, *90*, 445. (c) Chen, Y.; Rauk, A.; Tschuikow-Roux, E.; *J. Chem. Phys.* **1990**, *93*, 1187.
(60) (a) Truhlar, D. G.; Garrett, B. C. *Annu. Rev. Phys. Chem.* **1984**, *35*, 159. (b) Garrett, B. C.; Truhlar, D. G.; Schatz, G. C. *J. Am. Chem. Soc.* **1986**, *108*, 2876. (c) Zhang, J. Z. H.; Zhang, Y.; Kouri, D. J.; Garrett, B. C.; Haug, K.; Schwenke, D. W.; Truhlar, D. G. *Faraday Discuss. Chem. Soc.* **1987**, *84*, 371. (d) Lynch, G. C.; Halvick, P.; Truhlar, D. G.; Garrett, B. C.; Schwenke, D. W.; Kouri, D. J. *Z. Naturforsch.* **1989**, *44a*, 427.
(61) (a) Gold, V. *Trans. Faraday Soc.* **1964**, *60*, 739. (b) Pechukas, P. In *Dynamics of Molecular Collisions*; Miller, W. H., Ed.; Plenum Press: New York, 1976; Part B, p 269. (c) Pollak, E.; Pechukas, P. *J. Am. Chem. Soc.* **1978**, *100*, 2984. (d) Coulson, D. R. *Ibid.* **1978**, *100*, 2992. (e) Slanina, Z. *J. Mol. Struct. (THEOCHEM)* **1989**, *185*, 217. (f) Ischtwan, J.; Collins, M. A. *J. Chem. Phys.* **1991**, *94*, 7084. (g) Karas, J. A.; Gilbert, R. G.; Collins, M. A. *Chem. Phys. Lett.* **1992**, *193*, 181.
(62) Truhlar, D. G. *J. Comput. Chem.* **1990**, *12*, 266.
(63) Kilpatrick, J. E.; Pitzer, K. S. *J. Chem. Phys.* **1949**, *17*, 1064.
(64) Lewis, G. N.; Randall, M. *Thermodynamics*; revised by K. S. Pitzer and L. Brewer; McGraw-Hill: New York, 1961; pp 438-443.
(65) Garrett, B. C.; Truhlar, D. G. *J. Chem. Phys.* **1979**, *70*, 1593.
(66) Miller, W. H.; Handy, N. C.; Adams, J. E. *J. Chem. Phys.* **1980**, *72*, 99.
(67) Skodje, R. T.; Truhlar, D. G.; Garrett, B. C. *J. Phys. Chem.* **1981**, *85*, 3019.
(68) Kato, S.; Morokuma, K. *J. Chem. Phys.* **1980**, *73*, 3900.
(69) Wigner, E. Z. *Phys. Chem. B* **1932**, *19*, 203.
(70) Vaghjani, G. L.; Ravishankara, A. R. *Nature* **1991**, *350*, 406.